Experiments in Fluids 19 (1995) 61–68 © Springer-Verlag 1995

Low-Reynolds-number effects in a turbulent boundary layer

C. Y. Ching, L. Djenidi, R. A. Antonia

Abstract Low-Reynolds-number effects in a zero pressure gradient turbulent boundary layer have been investigated using a two-component LDV system. The momentum thickness Reynolds number R_θ is in the range 400 to 1320. The wall shear stress is determined from the mean velocity gradient close to the wall, allowing scaling on wall variables of the inner region of the layer to be examined unambiguously. The results indicate that, for the present R_θ range, this scaling is not appropriate. The effect of R_θ on the Reynolds normal and shear stresses is felt within the sublayer. Outside the buffer layer, the mean velocity is more satisfactorily described by a power-law than by a logarithmic distribution.

1 Introduction

The direct numerical simulation (DNS) boundary layer data of Spalart (1988) for R_θ in the range 300 to 1410 show that scaling on wall variables u_τ and ν (u_τ is the friction velocity and ν is the kinematic viscosity) is generally inappropriate for the inner region of the layer. Significant R_θ effects on the wall-normalized turbulence quantities are evident and often extend down to the wall. The wall-normalized Reynolds stresses exhibit different Reynolds number dependences, the w'^+ component (u, v, w denote the velocity fluctuations in the streamwise (x), wall-normal (y) and spanwise (z) directions respectively; the prime denotes an rms value, and the superscript + denotes normalization by the wall variables) being the most affected. Spalart's results show that, while u'^+ has a distinct peak at $y^+ \approx 15$, the peaks in v'^+, w'^+ and $-\overline{u^+v^+}$ are much broader, and their y^+ locations increase with R_θ. Similar low Reynolds number effects in the inner region of a fully developed turbulent channel flow have been observed both in experimental and DNS data (Kim et al. 1987; Wei and Willmarth 1989; Antonia et al. 1992). Using the channel flow DNS data, Antonia and Kim (1994) examined the near-wall behaviour of the various turbulence quantities; the asymptotic wall values of u'^+, v'^+, w'^+ and $-\overline{u^+v^+}$ were found to increase by 11, 29, 29 and 36 percent respectively when h^+ ($\equiv hu_\tau/\nu$, h is the channel half width) increased from 180 to 400. The corresponding increases for Spalart's DNS data are 8, 15, 19 and 16 percent when R_θ increases from 300 to 1410.

There is as yet no fully satisfactory explanation for these effects. Spalart (1988) attributed the effect to the inactive motion (Townsend 1961; Bradshaw 1967). Wei and Willmarth (1989) suggested two possible reasons: an increased vortex stretching with Reynolds number and a direct interaction between inner-region structures from opposite channel walls. Antonia et al. (1992), by introducing a small amount of heat at one of the walls in experiments and simulations, dismissed the direct interaction explanation as unlikely. They also found no significant evidence for attributing low Reynolds number effects to the inactive motion, arguing instead that the active motion should be the major contributor to the Reynolds shear and normal stresses in the inner region. Antonia and Kim (1994) concluded that low-Reynolds-number effects could be explained in terms of an intensification of the vortices in the wall region, although the average location and diameter of the vortices were approximately unchanged, when expressed in wall units.

Low Reynolds number effects are also discernible on the mean velocity. Spalart's data, when plotted in the form $(y^+ d\bar{U}^+/dy^+)$ versus y^+, suggest that R_θ effects extend into the inner region. On the basis of this plot, Spalart inferred that the log region disappears when R_θ is less than about 600. Arguments for a log region are strictly tenable only at infinite Reynolds number (e.g. Sreenivasan 1990), and there is no *a priori* reason for it to be valid at low Reynolds numbers. On the other hand, the arguments for a power law, $\bar{U}^+ = Cy^{+\alpha}$, which are as convincing as those for a log region (Barenblatt 1993; George and Castillo 1993), are valid at finite Reynolds numbers and should be more relevant for low R_θ boundary layers. In the outer region, the strength of the wake $\Delta\bar{U}^+$, defined by Coles (1962) as the maximum deviation of the velocity profile from the log region, has been shown to decrease for values of $R_\theta < 6000$ (most of the decrease occuring for $R_\theta < 2000$), and is often cited as an important indicator of low Reynolds number effects. However, in the light of the previous comments on the log region, $\Delta\bar{U}^+$ is unlikely to provide a reliable measure of low Reynolds number effects on the outer region.

Received: 6 September 1994/Accepted: 17 January 1995

C. Y. Ching, L. Djenidi, R. A. Antonia
Department of Mechanical Engineering,
University of Newcastle,
Newcastle, NSW 2308, Australia

Correspondence to: R. A. Antonia

The support of the Australian Research Council is gratefully acknowledged

The main aim of this study is to investigate low Reynolds number effects on the inner region of a turbulent boundary layer by exploiting the advantages of LDV in this region. At present, there are very few reliable measurements in the near-wall region of a turbulent boundary layer. This is primarily due to the difficulties associated with hot-wire anemometry in this region (e.g. see Antonia 1993). The reliability of near-wall LDV data can be ascertained from the boundary layer measurements ($R_\theta = 2400$) of Karlsson (1993). LDV allows the wall shear stress to be estimated from the mean velocity gradient close to the wall (Karlsson and Johansson 1988; Djenidi and Antonia 1993; Durst et al. 1993). This is particularly important when enquiring into the relevant scaling for both mean velocity and turbulence intensities in the inner layer.

2
Experimental details

The experiments were performed in a closed circuit constant-head vertical water tunnel (Zhou and Antonia 1992) shown schematically in Fig. 1. The vertical 2 m high working section (250 mm square cross section) is made of 20 mm thick clear perspex. One of the walls of the working section, which is removable, was used as the smooth wall. A roughness strip, which was made up of 4.5 mm high pebbles glued onto a 30 mm wide perspex strip, was recessed into a groove about 100 mm downstream from the exit of the contraction and used to trip the boundary layer. The measurement station was located about 1 m downstream of the roughness strip. Flow visualization performed by injecting dye through a hole in the wall indicated the boundary layer to be turbulent at this station for a freestream velocity, U_1, as small as 0.08 m/s. The maximum value of U_1 is about 0.5 m/s. The freestream turbulence intensity is less than 1% for all values of U_1. The pressure gradient was checked by measuring U_1 at several axial locations and found to be negligibly small ($U_1 dU_1/dx \approx 5.5 \times 10^{-4}\ \mathrm{ms}^{-2}$ for a freestream velocity of about 0.22 m/s).

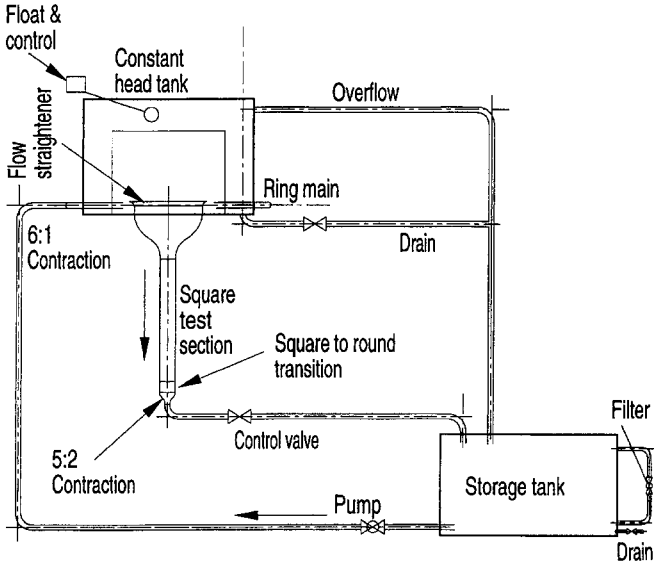

Fig. 1. Schematic of water tunnel

Measurements were performed at eight values of R_θ in the range 400 to 1320, corresponding to a range of 0.08 to 0.45 m/s for U_1. The stability of the tunnel during the relatively long experimental times ($\approx$ 8 hours for one profile) was confirmed by continuously monitoring the mean centerline velocity using a 15 mW He–Neon one-component TSI system.

For the boundary layer measurements, a three-component fibre optic LDV system (5W Ar-Ion) was used in forward scatter mode. Only two-component measurements for $u-v$ or $u-w$) were performed. Since refractive index effects are wavelength dependent, the two pairs of beams with the closest wavelengths (in this case, blue and violet with wavelengths 488 and 476.5 nm respectively) were used. For the $u-v$ measurements, the measuring volumes (0.04 mm × 0.5 mm for the blue beams and 0.04 mm × 0.9 mm for the violet beams) had their largest dimension oriented along the spanwise direction in order to optimize the spatial resolution (in the range 0.16 to 0.8 wall units) in the wall-normal direction. In this configuration, the beam closest to the wall (used for the wall-normal component) was centered using a pair of prisms, and the probe was slightly tilted ($\approx 2°$) with respect to the z-direction in order to obtain measurements very close to the wall. For the $u-w$ measurements, the length of the measuring volume (0.5 mm) was perpendicular to the wall, resulting in a spatial resolution (in the wall-normal direction) in the range 2 to 10 wall units. The probe was traversed using a three-dimensional computer-controlled traversing system, with a minimum step length of 0.025 mm in all three directions.

Enhanced Burst Spectrum Analyzers (BSA) were used for processing the photo multiplier signals. The two-component measurements were made in the coincidence mode, except very close to the wall where the data rates fall off quite steeply. In the coincidence mode, the two BSAs process the electrical signals only when the two signals are within the set coincidence time interval, allowing a more reliable measurement of the Reynolds shear stress $-\overline{uv}$. Very close to the wall, operation in the coincidence mode was not feasible because of the very low data rates. In this case, in order to improve the data rates, the BSAs were operated in the private mode whereby the signals are processed independently. Typical data rates in the outer part of the boundary layer were about 200 Hz, falling off to about 10 Hz very close to the wall. In the outer part of the boundary layer, 20000 samples were collected at each measurement point and this was reduced to 5000 samples very close to the wall.

To obtain correct $-\overline{uv}$ values, it is important that the velocity components that are being measured are associated with the same particle. Ideally, this is achieved by ensuring that the measuring volumes from the two pairs of transmitting beams overlap completely. However, because of the different sizes of the two measuring volumes and the orientation of the two pairs of beams, this is not easy to achieve in practice. It was determined that even a slight misalignment in any of the transmitting beams resulted in a large decrease in $-\overline{uv}$ (by as much as 35%). To ensure good overlap, alignment of the two measuring volumes was performed after taking into account the refractions of the transmitting beams due to the perspex and the water. The probe was set up in the same configuration as that used in the experiments, and a water-filled container fabricated from the same thickness perspex as the test section

was placed in front of the probe (this was necessary because of the lack of access to the test section itself). A 30 μm pinhole was placed in the water at the focusing point of the receiving optics, which was determined by guiding part of the laser light through the receiving fibre. The four transmitting beams were then adjusted so that their beam waists intersected at this point.

3 Determination of u_τ and mean velocity profiles

To examine the inner scaling laws unambiguously, an accurate estimate of the friction velocity is of paramount importance. At low R_θ, there is no rigorous basis for the log region, and the Clauser-plot technique would therefore be inaccurate for determining u_τ. The measurement of the mean velocity gradient, $d\bar{U}/dy$, at the wall should provide a more reliable estimate of u_τ. Djenidi and Antonia (1993) determined u_τ, with an estimated uncertainty of $\pm 3\%$, by fitting a straight line to their near-wall LDV data for $y^+ < 2.5$. This latter choice was based on the observation that the value of $d\bar{U}^+/dy^+$ (from the DNS data of Kim et al. 1987 and Spalart 1988) decreases to about 0.97, i.e. 3% below the wall value, at $y^+ \approx 2.6$.

For all R_θ, it was possible to obtain sufficient data in the region $y^+ < 2.5$ to allow u_τ to be estimated using the method of Djenidi and Antonia (1993). Close to the wall (roughly $y^+ \lesssim 12$), y-steps of 0.025 mm ($\Delta y^+ \approx 0.5$ for $R_\theta = 1316$) were used; this ensured that at least four data points were used for the linear fit. An initial estimate of u_τ was obtained by fitting a least squares straight line to the near-wall $\bar{U}$ data. The origin for the velocity profile was estimated by extrapolating this line to $\bar{U} = 0$; this location was always within ± 0.075 mm of the initial estimate of the origin (inferred by visual inspection of the intersection of the laser beams as they approached the perspex wall and of the analogue signals from the BSA's). From the initial estimate of u_τ, the physical values of y were converted to y^+ and a new linear fit was applied to all the data in the region $y^+ \leqslant 2.5$. The second (and final) estimate of u_τ was typically 5% larger than the first estimate; further iterations showed no change in the value of u_τ.

The error due to the velocity bias (McLaughlin and Tiederman 1973) was corrected by weighting the individual velocity realizations with their arrival times. An additional source of error is that due to the non-uniformity of the mean velocity distribution within the measuring volume. Durst et al. (1992) showed that, in the case of $\bar{U}$, this error is proportional to the square of the diameter of the measuring volume and to the second derivative $d^2\bar{U}/dy^2$. For the present beam configuration, the correction for this effect on $\bar{U}$ is less than 0.1 percent. The corrections for the rms quantities are also negligible. Very close to the wall, truncation of the measuring volume by the wall can introduce an additional error (Kried 1974). Djenidi and Antonia (1993) determined that this was not significant for the present set-up.

Normalized mean velocity profiles (Fig. 2; only three profiles are shown for clarity) show the same trend as the DNS profiles of Spalart. While the experimental data closely agree with the DNS data throughout the layer at the higher Reynolds number, they are slightly higher than the DNS data at the lower Reynolds numbers for $y^+ > 30$. There seems to be good collapse of the profiles in the region $y^+ \leqslant 30$; but a Reynolds number dependence is discernible for $y^+ > 30$. Note that only the collapse in the region $y^+ \leqslant 2.5$ is "forced" in view of the way in which u_τ is determined.

To accentuate the effects of R_θ on the mean velocity, especially in the inner region, $(y^+ d\bar{U}^+/dy^+)$ is plotted against $(\ln y^+)$ (Fig. 3). Such a plot represents a relatively critical test for the log region, which should appear as a plateau (see Spalart 1988). The derivative $d\bar{U}^+/dy^+$ was determined after first applying a curve fit to the data for $\bar{U}^+$. This was done via the calculation method of Bisset and Antonia (1991), which combines an eddy viscosity relation for the inner region and an empirical wake function for the outer region; the assumptions on which the calculation is based are not of particular relevance in the present context since the main interest here is to obtain a reliable curve fit to $\bar{U}^+$ in order to estimate $d\bar{U}^+/dy^+$ (thus avoiding the need to differentiate the $\bar{U}^+$ data). No significant plateau is evident in any of the $y^+ d\bar{U}^+/dy^+$ profiles. Instead, the profiles exhibit either a local minimum or a narrow plateau, indicating that a logarithmic region is either non-existent or very narrow. The value of $y^+ d\bar{U}^+/dy^+$ which corresponds to the minimum/plateau decreases as R_θ increases. Also, the position of the plateau

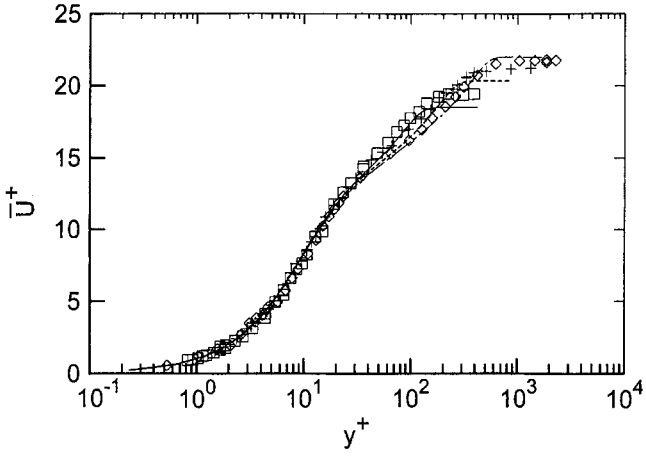

Fig. 2. Mean velocity. ◇, $R_\theta = 1316$; +, 765; □, 400; — — —, DNS 1410; – – – –, 670; ——, 300

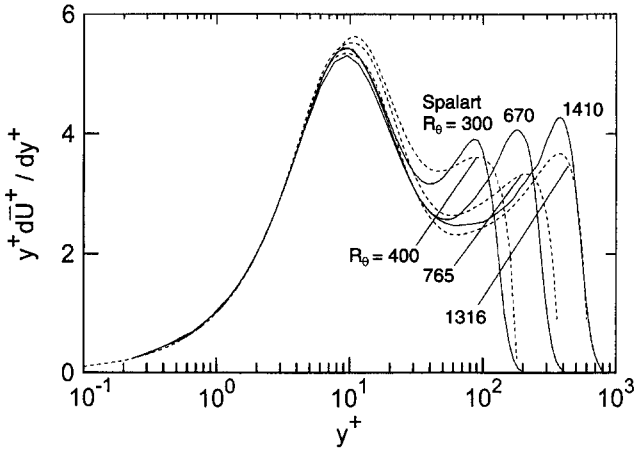

Fig. 3. Distribution of $(y^+ d\bar{U}^+/dy^+)$. ——, DNS; – – – –, experimental

tends to increase with R_θ. The distributions of $y^+ d\bar{U}^+/dy^+$ suggest that the effect of R_θ on $\bar{U}^+$ is discernible for $y^+ \geq 8$, i.e. the effect extends well into the buffer layer.

The mean velocity data are plotted in the form $(\bar{U}^+)^{1/\alpha}$ versus y^+ (Fig. 4) to ascertain whether a power-law distribution of the form

$$\bar{U}^+ = Cy^{+\alpha} + D, \tag{1}$$

is applicable. Arguing that the $[1/\ln(Re)]$ dependence displayed by the corrections to the classical Kolmogorov-Obukhov exponents 2/3 and 5/3 should be "a rather general property of developed turbulent flow, because it is based on general fractal properties of vortex dissipative structures in such flows", Barenblatt (1993) conjectured that the exponent α in (1) should display a similar Reynolds number dependence. Following Barenblatt (1993), the specific form for the exponent is

$$\alpha = \frac{3}{(2\ln R_\delta)}, \tag{2}$$

where R_δ ($\equiv U_1\delta/\nu$) is the boundary layer thickness Reynolds number. Straight lines are observed (Fig. 4) over the range

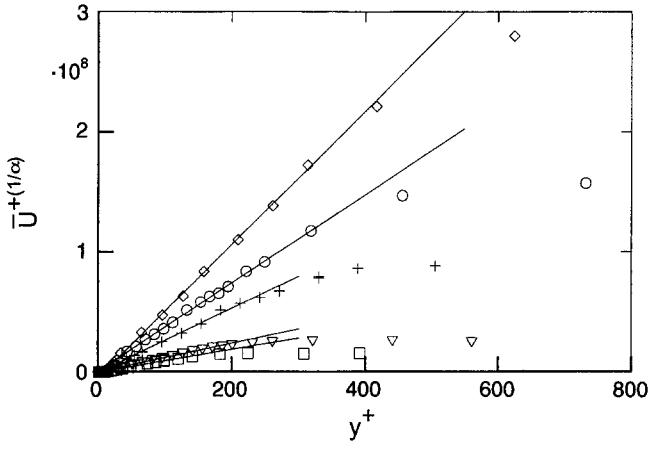

Fig. 4. Mean velocity plotted in the form of a power-law. ◇, $R_\theta = 1316$; ○, 979; +, 765; ▽, 509; □, 400; ——, least squares straight line fits

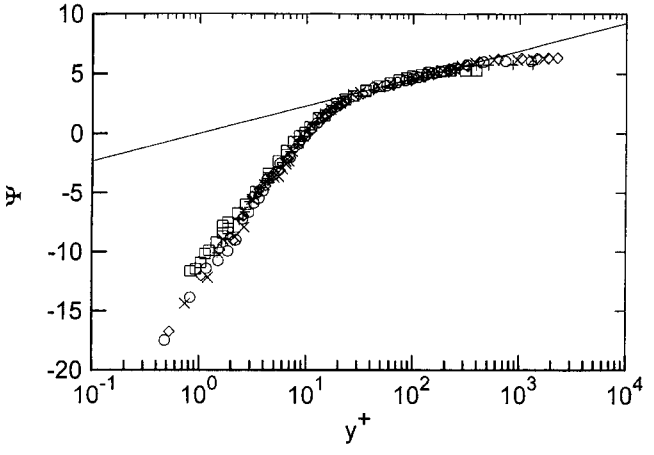

Fig. 5. Mean velocity plotted as a function $\Psi \equiv 1/\alpha \ln \bar{U}^+/C$. Symbols as for Fig. 4; ——, $\Psi = \ln y^+$

$30 < y^+ < 200$ for all R_θ, indicating that, beyond the buffer layer, $\bar{U}^+$ appears to be well represented by a power-law with α given by (2). When extrapolated, the straight lines in Fig. 4 (obtained by a least squares fit to the data in the region $30 < y^+ < 200$), go through the origin indicating that $D \approx 0$. A quasi-universal form of the power-law can be obtained by defining a new function Ψ (Barenblatt and Prostokishin 1993),

$$\Psi \equiv \frac{1}{\alpha} \ln \frac{\bar{U}^+}{C} = \ln y^+ . \tag{3}$$

Figure 5 indicates good agreement with (3) when $y^+ > 25$. This power-law extends well into the outer layer. Although the profiles deviate from the line $\Psi = \ln y^+$ for $y^+ < 25$ – this is expected since (1) is not supposed to be valid close to the wall – there is apparently good collapse of the data down to the sublayer. This collapse follows from the generally good collapse of $\bar{U}^+$ vs y^+ in the range $y^+ < 25$ (see Fig. 2), and the small variation of α and C over the present R_θ range ($0.158 < \alpha < 0.179$ and $7.51 < C < 8.03$).

4
Turbulence measurements

One measure of the uncertainty in the Reynolds stress measurements in the near-wall region ($y^+ \lesssim 15$) – there is a marked decrease in the signal-to-noise ratio as the wall is approached because of the decrease in the velocity itself, and the large amount of extraneous light (reflected from the wall) collected by the receiving optics – was provided by the scatter inferred by repeating measurements at the same y^+ location a number of times. This uncertainty (95% confidence – see Moffat 1988) was estimated at $\pm 4\%$ and $\pm 9\%$ for u' and v' respectively. The measurements for $-\overline{uv}$ in the region $y^+ \lesssim 15$ were found to be not reliable. An additional uncertainty is associated with the error in estimating the origin for y. Although this error is small (± 0.025 mm or an absolute error of the order of 0.1 to 0.5 wall units), this is highlighted in the near-wall region because of the logarithmic scale for y^+.

All of the u'^+ profiles (Fig. 6) have a discernible peak at about $y^+ = 15$; this location is consistent with that found for

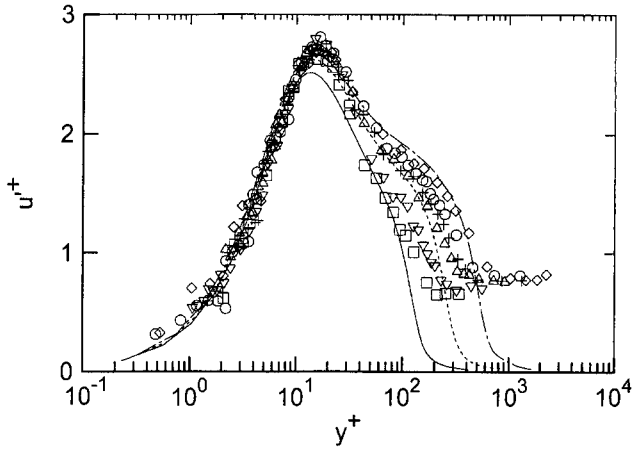

Fig. 6. rms longitudinal turbulence intensity. ◇, $R_\theta = 1316$; ○, 979; +, 765; △, 729; ▽, 509; □, 400; — – —, DNS 1410; – – – –, 670; ——, 300

the DNS data of Spalart (1988). The magnitude and y^+ location of the present u'^+_{max} is also in good agreement with the hot-wire data of Purtell et al. (1981) (these are not shown to avoid overcrowding). However, the nearly constant peak magnitude of about 2.75 is at variance with the systematic increase observed in the DNS data. For $y^+ > 15$, there is a generally systematic increase in u'^+ with R_θ at any given y^+; also, u'^+ falls off less rapidly with y^+ as R_θ increases. It is difficult to discern a Reynolds number effect from Fig. 6 in the region $y^+ < 15$. However, when only the near-wall data at the two extreme values of R_θ are plotted (Fig. 7), a systematic increase with R_θ is noticeable for both u'^+ and v'^+. The increase in v'^+ extends to larger values of y^+ than that in u'^+. In contrast to u'^+, the peak in v'^+ (Fig. 8) is much broader, and the magnitude and y^+ location of v'^+_{max} increase with R_θ. While the peak in u'^+ occurs at $y^+ \approx 15$, the peak location for v'^+ occurs in the range $60 < y^+ < 130$. A systematic increase in v'^+ with R_θ is observed for $y^+ > 15$, the increase being more pronounced than for u'^+. While it is difficult to discern any influence on R_θ in the region $y^+ < 15$ from Fig. 8, the results in Fig. 7 indicate that R_θ affects v'^+ well into the sublayer. Profiles of w'^+ are shown in Fig. 9, and for the range of y^+ in which the measurements were performed, show a systematic increase with R_θ. Note that relative to u'^+ and v'^+, the DNS data show that the effect of R_θ on w'^+ is much larger in the near-wall region. Despite the lack of near-wall measurements for w'^+, this trend is also evident in the experimental data; close to the wall, the poor spatial resolution in the wall-normal direction and the increased noise associated with the refraction of the laser beams through the wall (this is far more intense than the light scattered from the measuring volume) make it difficult to obtain good measurements. A peak in w'^+, albeit a broad one, is discernible in the range $30 < y^+ < 60$.

Distributions of the Reynolds shear stress $-\overline{u^+v^+}$ are presented in Fig. 10. The profiles show good agreement with the DNS data, and like v'^+, systematically increase with R_θ for $y^+ > 15$. Within the experimental uncertainty, it is difficult to determine the effect R_θ has on the region $y^+ \leqslant 15$. However, one would expect this effect to be present at the wall; both the channel and boundary layer DNS data show that $-\overline{u^+v^+}$ is more affected by R_θ than either u'^+ or v'^+. It can be surmised that the experimental difficulties (for $\overline{u^+v^+}$ the problems are exacerbated because of the difficulty of making coincidence mode measurements close to the wall) prevent the limiting wall behaviour of $-\overline{u^+v^+}$ to be resolved. The peak in $-\overline{u^+v^+}$ is

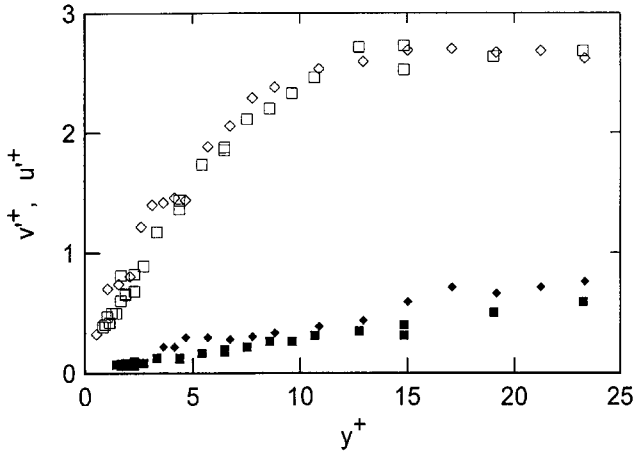

Fig. 7. Near-wall data for u'^+ and v'^+. ◇, $R_\theta = 1316$; □, 400. Open symbols for u'^+, solid symbols for v'^+.

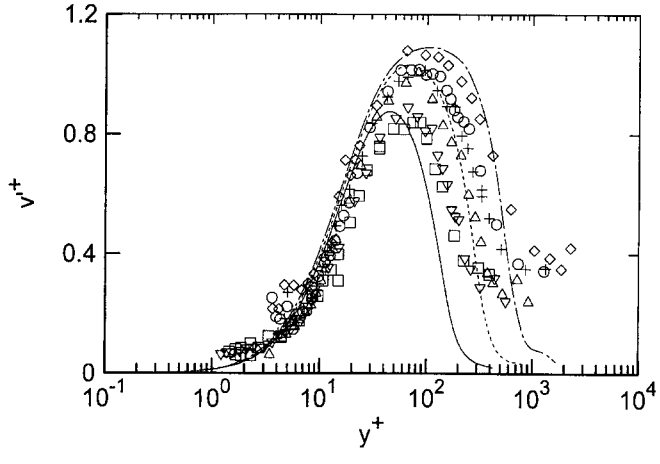

Fig. 8. rms normal turbulence intensity. Symbols and lines as for Fig. 6

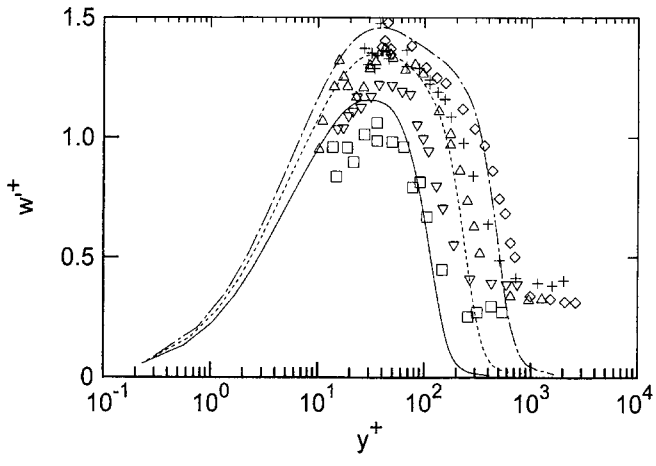

Fig. 9. rms spanwise turbulence intensity. Symbols and lines as for Fig. 6

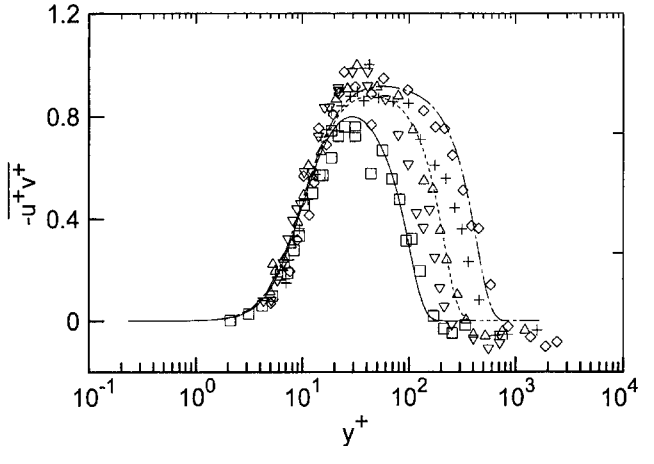

Fig. 10. Reynolds shear stress. Symbols and lines as for Fig. 6

broader than that for v'^+, and both its magnitude and y^+ location, notwithstanding the difficulty of defining this peak, increase with R_θ. However, the y^+ location ($30<y^+<60$) of $-\overline{u^+v^+}_{max}$ is smaller than that for v'^+_{max}. Sreenivasan (1990) found that the y^+ locations of v'^+_{max} and $-\overline{u^+v^+}_{max}$ may be approximated by

$$y^+_{v'_{max}} = (R^+)^{0.75} \tag{4}$$

and

$$y^+_{\overline{uv}_{max}} = 2(R^+)^{0.5} \tag{5}$$

where $R^+ \equiv u_\tau \delta / \nu$. The present data (Fig. 11) are in good agreement with (4) and (5) and with the turbulent channel flow data of Antonia et al. (1992). The correlation coefficient ρ_{uv} ($\equiv -\overline{uv}/u'v'$) displays a plateau with a value of about 0.4, starting at $y^+ \approx 10$ and extending well into the outer layer (Fig. 12). The scatter in the data makes it difficult to discern any systematic Reynolds number dependence for this parameter. However, the DNS data show that, throughout the layer, ρ_{uv} decreases as R_θ increases. Profiles of $-\overline{uv}$ normalized by $\overline{v^2}$ are presented in Fig. 13. The departure of the experimental data from the DNS data for $y^+ < 15$ is attributed to the difficulties in the $-\overline{u^+v^+}$ measurements in this region. There appears to be good collapse of the profiles in the range $15<y^+<100$. This reflects the fact that the increase in $-\overline{u^+v^+}$ with R_θ in this range is, to a large degree, offset by an increase in v'^+, suggesting that the mechanism responsible for the increase in $-\overline{u^+v^+}$ with R_θ must be the same as that for v'^+. This is plausible since the active motion should be the major contributor to both v'^+ and $-\overline{u^+v^+}$ (u'^+ receives contributions from the inactive motion – see Antonia et al. 1992), and the increase in these quantities is attributed to an intensification of the active motion with R_θ (Antonia and Kim 1994).

Profiles of the components of the Reynolds stress anisotropy tensor $b_{ij} \equiv \overline{u_i u_j}/2k - \delta_{ij}/3$ ($u_1 \equiv u$, $u_2 \equiv v$, $u_3 \equiv w$, $k \equiv \overline{u_i u_i}/2$ and δ_{ij} is the Kronecker delta, $=1$ when $i=j$ and $=0$ when $i \neq j$; repeated indices imply summation) are presented in Fig. 14 for $R_\theta = 400$ and 979. The lack of near-wall data for w'^+ precludes analysing the anisotropy of b_{ij} at the high end of the present R_θ range. The experimental data closely follow the DNS data, with b_{11} and b_{33} for $R_\theta = 400$ having a maximum and minimum respectively at $y^+ \approx 10$. The corresponding locations for

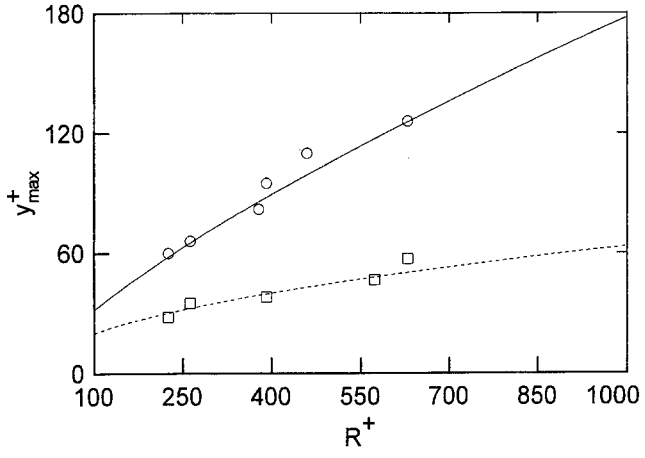

Fig. 11. Locations of maximum v'^+ and $-\overline{u^+v^+}$. ○, v'^+; □, $-\overline{u^+v^+}$; ——, Eq. (5); – – – –, Eq. (6)

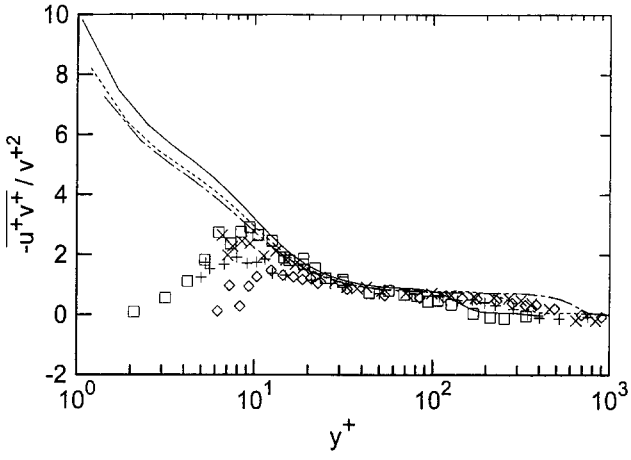

Fig. 13. Distribution of $-\overline{uv}/\overline{v^2}$. Symbols and lines as for Fig. 6

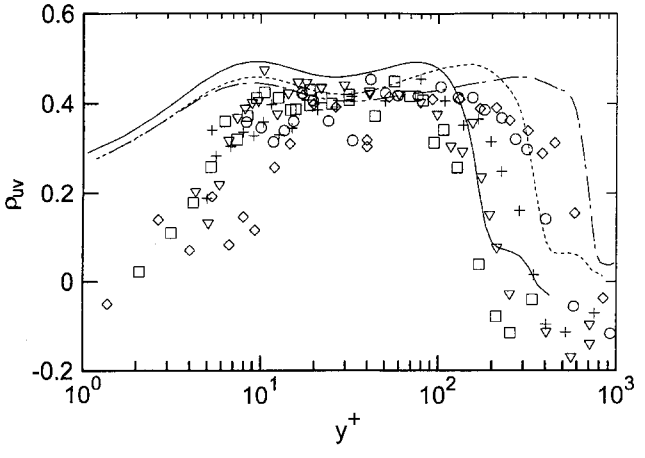

Fig. 12. Correlation coefficient between u and v. Symbols and lines as for Fig. 6

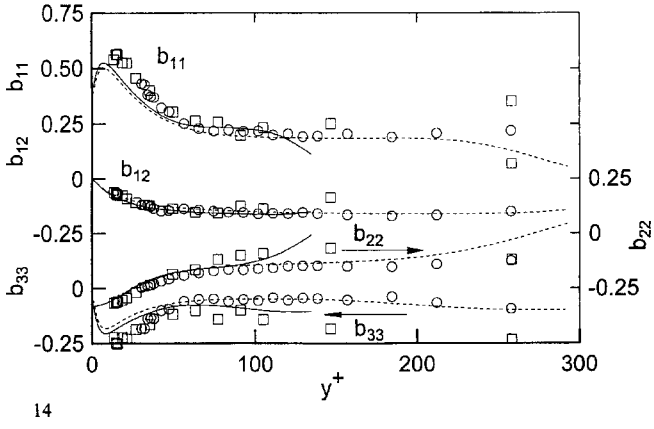

Fig. 14. Components of the Reynolds stress anisotropy tensor. Symbols and lines as for Fig. 6

the DNS data are at $y^+ \approx 8$. The cross-plot of the second ($II = -b_{ij}\,b_{ji}/2$) versus third ($III = b_{ij}\,b_{jk}\,b_{ki}/3$) invariants of b_{ij}, shown in Fig. 15, provides a useful framework for examining the flow anisotropy (see Antonia et al. 1994). The overall trend of the data is similar to that displayed by the DNS data. However, the experimental data display a higher degree of anisotropy than the DNS data, the largest anisotropy occuring at $y^+ \approx 10$. The data for $R_\theta = 400$ show that $-II$ and III reach maxima at this location (Fig. 16). There is insufficient near-wall data to comment on the effect of R_θ on the anisotropy. However, the DNS data exhibit increased anisotropy as the Reynolds number decreases. Antonia et al. (1994) attributed this to the increasing overlap between the energy containing large scales and the dissipative small scales as R_θ decreased.

As the freestream is approached, the values of u'^+, v'^+ and w'^+ (Figs. 6, 8 and 9) are at variance with the actual freestream turbulence intensity of about 1.0% (measured by Djenidi and Antonia (1993) using a 15 mW He–Neon one-component TSI system) This is directly attributed to noise (due to poor alignment of the beam waists) in the 2D probe when $(u'/\bar{U})$ is small. The probe used is a DANTEC 85 mm probe with a beam expander, and the beam separation distance was found to have a significant effect on this apparent turbulence intensity. Higher rms values were measured when the beam separation distance was reduced. Profiles of the Reynolds stresses measured with different beam separation distances showed that this effect decreases as $(u'/\bar{U})$ increases, and is not discernible when the value is greater than about 8%; the inner layer is thus relatively free of this error. The slightly negative values of $-\overline{u^+v^+}$ in the freestream (Fig. 10) are also spurious and are likely due to a slight misalignment of the beams with respect to the streamwise and wall-normal directions and/or a poor alignment of the beam waists within the probe. Subsequently, the probe was examined by the manufacturer and a slight degradation of the optical fibre ends was found due to particle deposit. Measurements of $(u'/\bar{U})$ taken after the optical fibres were replaced show that, while the values in the freestream are reduced to about 1 percent, the inner region values remain essentially unchanged.

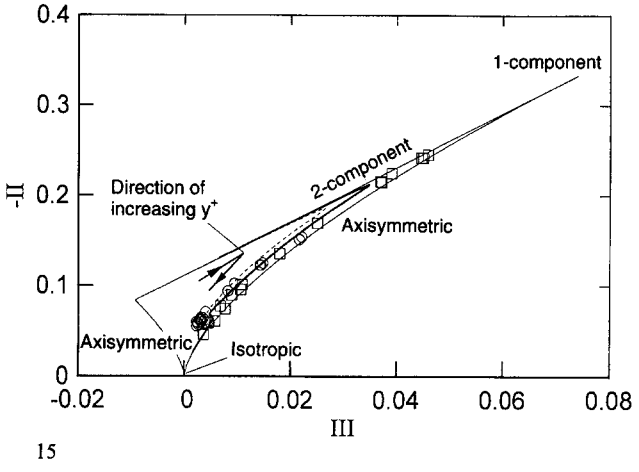

Fig. 15. Cross-plot of second and third invariants of the Reynolds stress anisotropy tensor. Symbols and lines as for Fig. 6

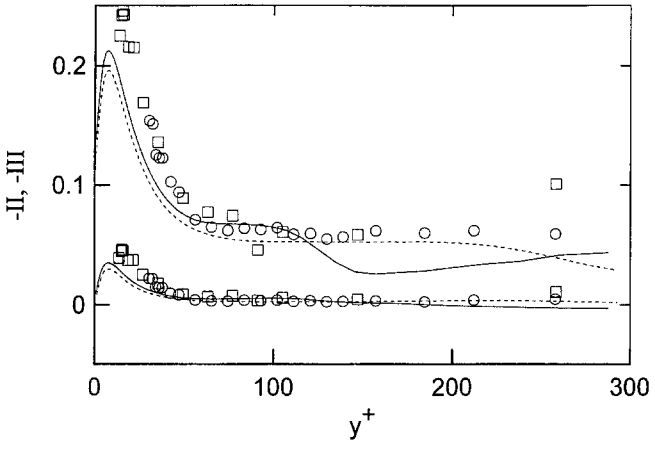

Fig. 16. Second and third invariants of the Reynolds stress anisotropy tensor. Symbols and lines as for Fig. 6

5
Conclusions

The present LDV investigation of a turbulent boundary layer indicates that there are significant low Reynolds number effects on the mean velocity and Reynolds stresses. This is in conformity with the conclusions drawn by Spalart (1988) on the basis of a direct numerical simulation of this flow.

1. The profiles of $(y^+ d\bar{U}^+/dy^+)$ suggest that R_θ affects the mean velocity in the region $y^+ \gtrsim 8$. Outside the buffer layer, the mean velocity is well described by a power-law, as opposed to a universal log-law.
2. The near-wall data for u'^+ and v'^+ show that the R_θ effect extends well into the sublayer, indicating that, in the range $400 \leqslant R_\theta \leqslant 1320$, scaling on wall variables is, in general, not appropriate.
3. The dependence of each wall-normalized quantity on the Reynolds number is different. While the peak in u'^+ is distinct and its magnitude and y^+ location are nearly constant, the peaks in v'^+, w'^+ and $-\overline{u^+v^+}$ are much broader and both the magnitude and location increase with R_θ.
4. There appears to be good collapse of the $-\overline{uv}$ profiles when normalized by $\overline{v^2}$ in the range $15 < y^+ < 100$, indicating that the increase in $-\overline{u^+v^+}$ with R_θ is, to a large degree, offset by an increase in v'^+ in this region. This is consistent with the notion that the active motion is the major contributor to both v'^+ and $-\overline{u^+v^+}$, and that the increase in these quantities is attributed to an intensification of the active motion with R_θ.
5. The experimental data for $R_\theta = 400$ display a higher degree of anisotropy of the Reynolds stress tensor than the DNS data. The anisotropy is maximum at $y^+ \approx 10$.

References

Antonia RA (1993) Direct numerical simulations and hot wire experiments: A possible way ahead? In: New approaches and concepts in turbulence (ed. T. Dracos and A. Tsinober), Birkhäuser Verlag, Basel, Switzerland, 349–365

Antonia RA; Djenidi L; Spalart PR (1994) Anisotropy of the dissipation tensor in a turbulent boundary layer. Phys Fluids 6: 2475–2479

Antonia RA; Kim J (1994) Low Reynolds number effects on near-wall turbulence. J Fluid Mech 276: 61–80

Antonia RA; Teitel M; Kim J; Browne LWB (1992) Low-Reynolds-number effects in a fully developed turbulent channel flow. J Fluid Mech 236: 579–605
Barenblatt GI (1993) Scaling laws for fully developed turbulent shear flows. Part 1. Basic hypotheses and analysis. J Fluid Mech 248: 513–520
Barenblatt GI; Prostokishin VM (1993) Scaling laws for fully developed turbulent shear flows. Part 2. Processing of experimental data. J Fluid Mech 248: 521–529
Bisset DK; Antonia RA (1991) Mean velocity and Reynolds shear stress in a turbulent boundary layer at low Reynolds numbers. Aeron Quart 95: 244–247
Bradshaw P (1967) 'Inactive' motion and pressure fluctuations in turbulent boundary layers. J Fluid Mech 30: 241–258
Coles DE (1962) The turbulent boundary layer in a compressible fluid. Rand report R-403-PR
Djenidi L; Antonia RA (1993) LDA measurements in a low Reynolds number turbulent boundary layer. Exp Fluids 14: 280–283 (see also Erratum, Exp Fluids 15, 386).
Durst F; Jovanovic J; Sender J (1993) Detailed measurements of the near wall region of turbulent pipe flows. Ninth Symposium on Turbulent Shear Flows, Kyoto, Japan, 2.2.1–2.2.3
Durst F; Martinuzzi R; Sender J; Thevenin D (1992) LDA Measurements of mean velocity, RMS-values and higher order moments of turbulence intensity fluctuations in flow fields with strong velocity gradients. Sixth International Symposium on Applications of Laser Techniques to Fluid Mechanics, Lisbon, Portugal
Erm L; Joubert PN (1991) Low Reynolds Number turbulent boundary layers. J Fluid Mech 230: 1–44
George WK; Castillo L (1993) Boundary layers with pressure gradient: Another look at the equilibrium boundary layer. In: Near-wall turbulent flows (ed. R.M.C. So, C.G. Speziale and B.E. Launder), Elsevier Science Publishers, 901–910
Karlsson RI (1993) Near-Wall measurements of turbulence structure in boundary layers and wall jets. In: Near-wall turbulent flows (ed. R.M.C. So, C.G. Speziale and B.E. Launder), Elsevier Science Publishers, 423–432
Karlsson RI; Johansson TG (1988) LDV measurements of higher order moments of velocity fluctuations in a turbulent boundary layer. In: Laser anemometry in fluid mechanics III (ed. R.J. Adrian et al.), Ladoan-Instituto Superior Tecnico, Portugal, 273–289
Kim J; Moin P; Moser R (1987) Turbulence statistics in fully developed channel flow at low Reynolds number. J Fluid Mech 177: 133–166
Kried DK (1974) Laser doppler velocimeter measurements in nonuniform flow: Error estimates. Appl Opt 13: 1872–1881
McLaughlin DK; Tiederman WG (1973) Biasing correction for individual realization of laser anemometer measurements in turbulent flows. Phys Fluids 16: 2082–2088
Moffat RJ (1988) Describing the uncertainties in experimental results. Exp Thermal and Fluid Science 1: 3–17
Purtell LP; Klebanoff PS; Buckley FT (1981) Turbulent boundary layers at low Reynolds numbers. Phys Fluids 24: 802–811
Spalart PR (1988) Direct simulation of a turbulent boundary layer up to $R_\theta = 1410$. J Fluid Mech 187: 61–98
Sreenivasan KR (1990) The turbulent boundary layer. In: Frontiers in Experimental Fluid Mechanics (ed. M. Gad-el-Hak) pp 159–210, Springer-Verlag
Townsend AA (1961) Equilibrium layers and wall turbulence. J Fluid Mech 11: 97–120
Wei T; Willmarth WW (1989) Reynolds-number effects on the structure of a turbulent channel flow. J Fluid Mech 204: 57–95
Zhou Y; Antonia RA (1992) Convection velocity measurements in a cylinder wake. Exp Fluids 13: 63–70

Announcement

The ninth international symposium on transport phenomena (ISTP-9) in thermal-fluids engineering, June 25–28, 1996, Singapore

Scope

Papers which deal with any aspects of transport phenomena in thermal-fluids engineering from fundamental sciences to applied technologies are invited. Topics include but are not limited to:

- Boundary layer flows
- Free shear flows
- Turbulence and flow instabilities
- Computational fluid dynamics
- Experimental fluid dynamics
- Industrial aerodynamics and wind engineering
- Heat and mass transfer
- Heat exchangers
- Combustion and reacting flows
- Environmental systems
- Chemical process systems
- Advanced energy systems
- Electronic equipment cooling
- Thermal-fluids machinery
- Bioengineering
- Biothermal fluid dynamics
- Special topics

Selection of papers

Initial screening will be based on the abstract of approximately 500 English words. The abstract should contain: 1) paper title, 2) five keywords in the order of importance and 3) name, address, phone number, and fax number of the author to whom subsequent correspondence should be directed. The abstract should state clearly the objectives, results and conclusions to enable the scope and nature of the paper to be assessed. Final acceptance will be based on review of the complete manuscript. All papers to be presented will be included in bound volume(s) which will be available at the meeting.

Conference secretariat

All correspondence should be addressed to:

ISTP-9 Secretariat
Ken-Air Destination Management Co Pte Ltd.,
257 Selegie Road #03-275 Selegie Complex,
Singapore 0718,
Republic of Singapore

Tel.: (65) 3368855 Fax: (65) 3363613

Deadlines

Four (4) copies of abstract due:	August 15, 1995
Notification of abstract acceptance:	August 31, 1995
Four (4) copies of full length paper due for review:	October 31, 1995
Notification of paper acceptance:	January 15, 1996
Camera-ready manuscript together with advance registration and accommodation reservation:	February 29, 1996